Journal Pre-proof

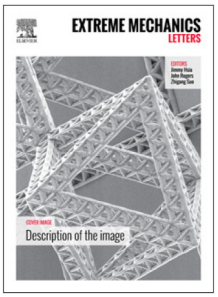

Adhesive rolling of nanoparticles in a lateral flow inspired from diagnostics of COVID-19

Huilin Ye, Zhiqiang Shen, Ying Li

PII: S2352-4316(21)00041-9
DOI: https://doi.org/10.1016/j.eml.2021.101239
Reference: EML 101239

To appear in: *Extreme Mechanics Letters*

Received date : 5 October 2020
Revised date : 1 February 2021
Accepted date : 17 February 2021

Please cite this article as: H. Ye, Z. Shen and Y. Li, Adhesive rolling of nanoparticles in a lateral flow inspired from diagnostics of COVID-19, *Extreme Mechanics Letters* (2021), doi: https://doi.org/10.1016/j.eml.2021.101239.

Adhesive Rolling of Nanoparticles in a Lateral Flow Inspired from Diagnostics of COVID-19

Huilin Ye, Zhiqiang Shen, Ying Li*

Department of Mechanical Engineering and Polymer Program, Institute of Materials Science, University of Connecticut, Storrs, CT 06269, USA

Abstract

Due to the lack of therapeutics and vaccines, diagnostics of COVID-19 emerges as one of the primary tools for controlling the spread of SARS-COV-2. Here we aim to develop a theoretical model to study the detection process of SARS-COV-2 in lateral flow device (LFD), which can achieve rapid antigen diagnostic tests. The LFD is modeled as the adhesion of a spherical nanoparticle (NP) coated with ligands on the surface, mimicking the SARS-COV-2, on an infinite substrate distributed with receptors under a simple shear flow. The adhesive behaviors of NPs in the LFD are governed by the ligand receptor binding (LRB) and local hydrodynamics. Through energy balance analysis, three types of motion are predicted: i) firm-adhesion (FA); ii) adhesive-rolling (AR); and iii) free-rolling (FR), which correspond to LRB-dominated, LRB-hydrodynamics-competed, and hydrodynamics-dominated regimes, respectively. The transitions of FA-to-AR and AR-to-FR are found to be triggered by overcoming LRB barrier and saturation of LRB torque, respectively. Most importantly, in the AR regime, the smaller NPs can move faster than their larger counterparts, induced by the LRB effect that depends on the radius R of NPs. In addition, a scaling law is found in the AR regime that $v \propto \dot{\gamma} R^{\alpha}$ (rolling velocity v and shear rate $\dot{\gamma}$), with an approximate scaling factor $\alpha \sim -0.2 \pm 0.05$ identified through fitting both theoretical and numerical results. The scaling factor emerges from the energy-based stochastic LRB model, and is confirmed to be universal by examining selections of different LRB model parameters. This size-dependent rolling behavior under the control of flow strength may provide the theoretical guidance for designing efficient LFD in detecting infectious disease.

Keywords: COVID-19, diagnostics, micro-/nano-fluid dynamics, nanoparticle adhesion

*Corresponding authors.
Email addresses: yingli@engr.uconn.edu (Y.L.)

1. Introduction

Diagnostics of COVID-19 is the primary tool to control the spread of SARS-COV-2 after the report of the first case in Wuhan City (China) [1], due to the lack of effective therapeutics and vaccines. Current diagnostic methods have three main approaches: nucleic acid amplification tests (NAATs), antigen-directed virus detection, and serological assays [2, 3, 4]. Among them, rapid antigen diagnostic tests, usually based on lateral flow device (LFD), have expanded widely due to its inexpensive, fast, qualitative and point-of-care testing [5, 6]. Although LFD demonstrates fast detection, the accuracy and sensitivity are limited compared to the NAATs. This low reliability may in part due to the inaccurate control of the flow and inadequate understanding of the interaction between antibody and antigen under the flow environment.

To improve the reliability of LFD, attentions are paid to focus on the ligand-receptor binding (LRB) process [2, 5, 6, 7, 8]. In LFD analysis, the viruses are usually modeled as nanoparticles (NPs) coated with ligands on the surface, as presented in Fig. 1(a). The detection is conducted through the capture of ligands by the biological receptors on the substrate. Typically, there are three types of motion of NPs on the substrate: initial contact; adhesive rolling on substrate; and final firm-adhesion. These kinetic processes are strongly determined by the size-dependent physiological (Stokes' drag) and biophysical (LRB) conditions. Extensive efforts have been made to study the adhesion behaviors of NPs [9, 10, 11, 12]. Nevertheless, the complex interplay between hydrodynamics, Brownian motion, and stochastic LRB hinders the progress of investigations on NPs subjected to flow conditions.

Although numerical simulations have been conducted to investigate the transport of NPs in fluid environment, the focuses are centered around either suspension rheology [13, 14, 15, 16] or thermal fluctuation of a single NP [17, 18, 19]. For instance, [18] adopted the fluctuating hydrodynamics approach to study the motion of nano-sized spheroid in a cylindrical vessel flow. The effects of geometries such as shape and aspect ratio of NPs on their velocity and angular velocity autocorrelations as well as diffusivities have been uncovered. Nevertheless, corresponding studies that account for the stochastic LRB towards vessel wall have largely remained unexplored [20, 21].

On the other side, researches on adhesive motion of cells that are much larger than NPs in the flow condition have attracted extensive attentions during the past decades, due to its important role in many fundamental biological processes such as cell growth [22], migration [23] and differentiation [24]. A typical example is the migration and adhesion of leukocytes during the inflammatory process [25]. The circulating leukocytes in blood flow initially interact with the endothelium cells through LRB and then roll on the endothelium until they eventually stop on the inflammatory site. This process involves three types of motion: free-rolling in blood flow, adhesive-rolling on the endothelium, and firm-adhesion on the disease site [26]. It is found that the transition from firm-adhesion to adhesive-rolling can happen when the shear rate exceeds a threshold [27]. However, a lower threshold that characterizes the transition from adhesive-rolling to firm-adhesion is recently observed [28].

This bistability is also confirmed by *in vitro* experiments [29] and theoretical analysis [30]. In the corresponding theoretical work, the models that describe the kinetics of cell rolling on the vessel wall under laminar shear flow have been established by torque and energy balance analyses. Although the target is cell instead of NP and the analysis is limited to two-dimensional circumstance, the theoretical approach such as energy balance may shed light on the corresponding studies of the adhesive motion of NPs in shear flow.

Inspired by above aspects, we theoretically investigate the adhesion of a spherical NP on an infinite substrate under LRB and simple shear flow through energy balance analysis. The motion of NP is assumed to be determined by the interplay of LRB and local hydrodynamics. Similar to leukocytes, three types of motion are predicted: i) firm-adhesion (FA); ii) adhesive-rolling (AR); and iii) free-rolling (FR), which correspond to LRB-dominated, LRB-hydrodynamics-competed, and hydrodynamics-dominated regimes, respectively. More importantly, we find that small NPs can move much faster than their larger counterparts in the AR regime, which is contradictory to the Stokes' prediction that larger particles will experience larger torque in shear flow and move faster [31]. Through both theoretical analysis and numerical simulations, we identify that this contradiction is induced by the LRB, which slows down the movement of large size NPs in shear flow. With the shear rate increasing, the Stokes' prediction is fully recovered and the motion of NPs is dominated by local hydrodynamics. This size-dependent rolling behavior may provide theoretical guidance for broad applications of LFD in detecting various viruses with different sizes such as Severe Acute Respiratory Syndrome (SARS) and Middle East Respiratory Syndrome (MERS), and SARS-COV-2 [5].

2. Theoretical Analysis

In our theoretical model, a spherical NP with radius R and density ρ^s is placed above an infinite rigid substrate as shown in Fig. 1(b). The surface of the NP is coated with ligands and the receptors are distributed on the substrate. The NP is immersed in a semi-infinite simple shear flow bounded by the substrate. The viscosity and shear rate of the flow are η and $\dot{\gamma}$, respectively. We fix the environmental temperature of this system at $T = 310\ K$. It is assumed that the distributions of ligands and receptors are uniform, and their densities are n_l and n_r, respectively. When the NP moves close to the substrate, the ligands and receptors can interact with each other and then they might bind together to form biological bonds as depicted in Fig. 1(b).

Under the shear flow, besides the LRB, the NP also experiences hydrodynamics and thermal fluctuation. The thermal fluctuation is attributed to the ambient fluid, acting as heat reservoir with temperature T. The Péclet number is defined as $Pe = 2Ru_{\max}/D_\infty$, where $u_{\max} = \dot{\gamma}R$ corresponds to the maximum flow velocity around the NP and $D_\infty = \frac{k_{\mathrm{B}}T}{6\pi\eta R}$ is the Stokes-Einstein diffusivity. k_B is the Boltzmann constant. Since the minimum size of NP we study here is $R = 40$ nm and the shear rate of flow has the order $\dot{\gamma} \sim 10^{-4}$ ns^{-1}, the Péclet number corresponds to the order $Pe = \frac{12\pi\eta\dot{\gamma}R^3}{k_{\mathrm{B}}T} \sim 10^5$ that indicates the thermal

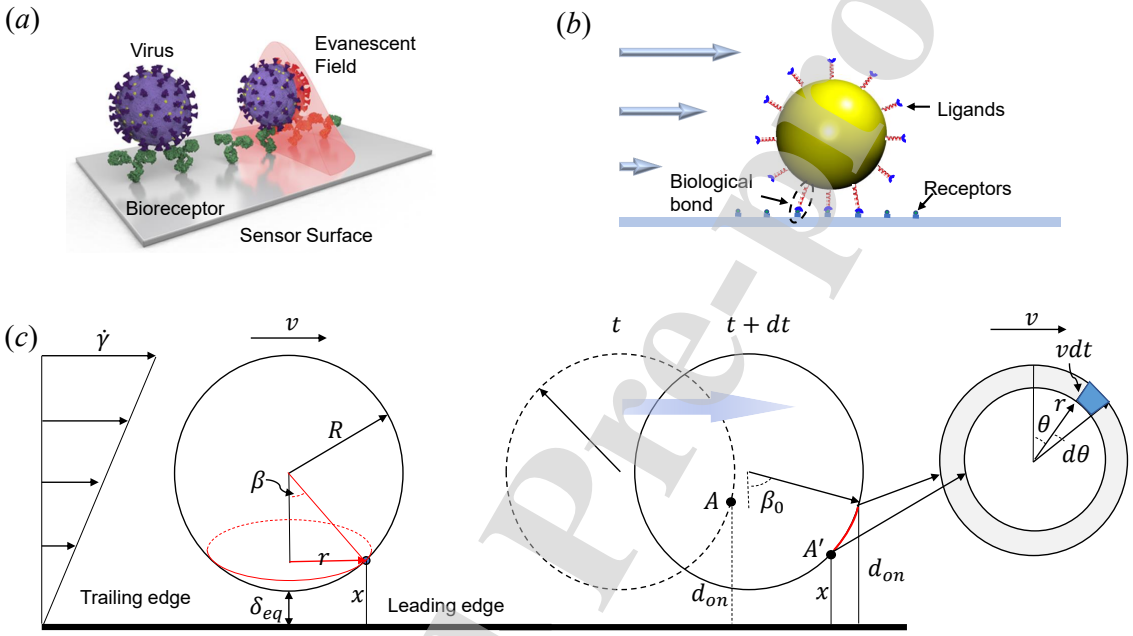

Figure 1: (a) Schematic of diagnostics of respiratory virus infections, adapted from Ref. [5] (Copyright 2020 ACS). (b) Schematic of a spherical NP on substrate under ligand-receptor binding in a simple shear flow. (c) Theoretical model. The shear rate of the simple shear flow is $\dot{\gamma}$. R is the radius of the NP, v is the moving velocity of the NP, δ_{eq} represents the equilibrium length of the ligand receptor bond, x is the distance between ligand and receptor, r is the corresponding radius of the crossed circle and β is the angle with shear direction. d_{on} is the cutoff of the ligand receptor interaction, and A is the corresponding critical position at time t, which has a angle β_0 with the shear direction. And at time $t + dt$, A moves to A'. The ring on the plane is the projection of the moving area (denoted by red line) in the 3D configuration of spherical NP, which describes the movement of NP at time dt on the substrate. θ in the moving part is defined as the angle between the r and vertical direction.

fluctuation can be negligible. To confirm this, we still include the thermal fluctuation effect in the numerical simulations, and we find it contributes to the motion of NPs significantly only when the shear rate is extremely small (low Péclet number, cf. Appendix B). However, for simplicity, the thermal fluctuation is not considered in the theoretical analysis. Through removing the thermal fluctuation, the NP's motion is governed by the competition between hydrodynamics and LRB. Through this competition, the NP can present either rolling or static on the substrate. For the theoretical analysis, we assume the NP keeps rolling with velocity v on the substrate with no slipping, therefore, $v = R\omega$ with the angular velocity ω. The kinetic energy of the NP is

$$E(t) = \frac{1}{2}mv^2(t) + \frac{1}{2}I_{cm}\omega^2(t) = \frac{1}{2}J\omega^2(t), \tag{1}$$

where I_{cm} is the inertial moment, and $J = mR^2 + I_{cm}$. The hydrodynamic work exerted on the NP done by the shear flow in the time interval $(0, t)$ is

$$W_h(t) = \int_0^t F_h(\tau)v(\tau)d\tau + \int_0^t M_h(\tau)\omega(\tau)d\tau, \tag{2}$$

where F_h and M_h are hydrodynamic force and torque, respectively.

The work consumed by the LRB can be described as

$$W_{\mathrm{LR}}(t) = \int_0^t M_{\mathrm{LR}}(\tau)\omega(\tau)d\tau, \tag{3}$$

where M_{LR} is the torque exerted on the NP due to LRB. We assume the NP is initially static, then we have the energy balance form:

$$W_h(t) = E(t) + W_{\mathrm{LR}}(t), \tag{4}$$

which can be expressed as

$$\begin{aligned}\frac{1}{2}J\omega^2(t) + \int_0^t M_{\mathrm{LR}}(\tau)\omega(\tau)d\tau = &\int_0^t F_h(\tau)v(\tau)d\tau \\ &+ \int_0^t M_h(\tau)\omega(\tau)d\tau.\end{aligned} \tag{5}$$

Taking the derivation with respect to t, we have

$$\frac{J}{R}\frac{dv(t)}{dt} + M_{\mathrm{LR}} = F_hR + M_h. \tag{6}$$

Assuming the NP reaches a steady state, saying $\frac{dv(t)}{dt} = 0$, then we have the governing equation of the steady motion for the NP

$$M_{\mathrm{LR}} = F_hR + M_h. \tag{7}$$

In the following, we restrict our discussion to the steady motion of NP unless otherwise stated.

To gain insights into the motion of NP, the concrete expression of the Eq. (7) needs to be further deduced. Firstly, based on Stokes' law [32], [31] derived the exact solution of Stokes' equations for a sphere moving near a plane wall under simple shear flow. According to [31], the force and torque that the NP experiences in the flow are:

$$F_h = 6\pi\eta R(F_s^*\dot{\gamma}h - F_t^* v), \quad M_h = 8\pi\eta R^3(T_s^*\dot{\gamma} - T_r^*\frac{v}{R}), \tag{8}$$

where F_s^* and F_t^* are hindered force coefficients induced by flow and translation of NP. Similarly, T_s^* and T_r^* are hindered torque coefficients led by flow and rotation of NP. Furthermore, the empirical expressions of the coefficients are provided: $F_s^* = 1 + \frac{9}{16}\Lambda, F_t^* = (1 - \frac{9}{16}\Lambda)^{-1}, T_s^* = 1 - \frac{3}{16}\Lambda^3$ and $T_r^* = 1 + \frac{5}{16}\Lambda^3$, where $\Lambda = R/h$, and h is the distance between the center of NP and the substrate. Although the confinement of the substrate can affect the motion of NP, it is obvious that, from the force and torque expressions, the nature of Stokes' prediction that larger particles will move faster than smaller ones in simple shear flow is maintained.

Secondly, the LRB is characterized by the biological bonds formed between ligands and receptors. In our model, the biological bond association and dissociation are governed by the probabilistic adhesion model developed by [33] based on the Bell model [34]. This model has been widely used in describing cell and NP adhesive behaviors and has performed well in terms of the accuracy and simplicity [35, 36, 37, 20]. When a ligand on the NP surface is close to a receptor on the substrate within a characteristic length d_{on}, there is a probability P_{on} to create a new biological bond between them. Reversely, an existing bond suffers a breakup probability P_{off} within a critical length d_{off}. The probabilities are mathematically defined as

$$P_{\text{on}} = \begin{cases} 1 - e^{-k_{\text{on}}\Delta t}, & l < d_{\text{on}} \\ 0, & l \geq d_{\text{on}} \end{cases}, \quad P_{\text{off}} = \begin{cases} 1 - e^{-k_{\text{off}}\Delta t}, & l < d_{\text{off}} \\ 1, & l \geq d_{\text{off}} \end{cases}, \tag{9}$$

where k_{on} and k_{off} are the association and dissociation rates, respectively. They have the forms: $k_{\text{on}} = k_{\text{on}}^0 \exp(-\frac{\sigma_{\text{on}}(l-l_0)^2}{2k_{\text{B}}T})$, $k_{\text{off}} = k_{\text{off}}^0 \exp(\frac{\sigma_{\text{off}}(l-l_0)^2}{2k_{\text{B}}T})$, where σ_{on} and σ_{off} are the effective on and off strengths, denoting a decrease and increase of the corresponding rates within the interaction lengths d_{on} and d_{off}, respectively. $k_{\text{B}}T$ is the energy unit. k_{on}^0 and k_{off}^0 are association and dissociation rates at the equilibrium length $l = l_0$ between ligand and receptor, respectively. l_0 represents the equilibrium length of the biological bond. Thus, the force of a biological bond is: $F^b = k_s(l - l_0)$, which will exert on both receptor and ligand, but with different directions along with the bond. Here, k_s is the bond strength which is attributed to the rupture energy $E_r = -\frac{1}{2}k_s\Delta x_m^2$ that is required to break up a single bond. Δx_m is the maximum extension of the bond. Δt in the expressions is the time step in both theoretical analysis and computer simulation. Note that only a single bond is allowed to form at each ligand or receptor. The selection of parameters in the LRB process and the corresponding references are listed in Table 1.

Parameters	Physical Value	References
l_0	10 nm	[11]
$E_{\mathrm{r}}(-\frac{1}{2}k_s\Delta x_m^2)$	$-45\ k_{\mathrm{B}}T \sim -17\ k_{\mathrm{B}}T$	[38]
$d_{\mathrm{on}}/d_{\mathrm{off}}$	40 nm	[39]
σ_{on}	0.1 pN/nm	[40]
σ_{off}	0.2 pN/nm	[40]
k_{on}^0	0.8 ns^{-1}	[41]
k_{off}^0	5×10^{-4} ns^{-1}	[41]
n_l	0.023 $\mathrm{mol/nm}^2$	[11]
n_r	0.01 $\mathrm{mol/nm}^2$	[11]

Table 1: Parameters used in the adhesive model for ligand-receptor binding.

At time t, the NP is in torque-free state and the biological bonds are called 'closed bonds' under this state. When the NP starts to move, the LRB torque is induced by the imbalance between the association torque of leading edge led by newly formed bonds and the dissociation torque of trailing edge induced by stretching of closed bonds. In the following, we strive to find the analytical expressions of association torque and dissociation torque by geometrical analysis. The smallest distance between NP and substrate is defined as δ_{eq} (cf. Fig. 1(c)). x denotes the distance of ligand from the substrate and r is the corresponding radius of the crossed circle. β is the angle with shear direction as shown in Fig. 1(c). Similarly, β_0 is the angle between the critical position where the ligand has a distance d_{on} from the substrate and shear direction. We track the critical point A (distance d_{on} from te substrate) at the leading edge of the NP from t to $t+dt$. At time $t+dt$, it will move to the position A' with distance x from the substrate. We project this part (denoted as red line in Fig. 1(c)) of the NP on the substrate, it is nearly a ring region, namely influence region, with intra radius $r=\sqrt{R^2-(R+\delta_{\mathrm{eq}}-x)^2}$ and width vdt is the displacement of point A within time dt. Inside this region, there are new interactions between ligands and receptors. x can be expressed as $R(1-\cos(\beta_0-\frac{vdt}{R}))+\delta_{\mathrm{eq}}$. In the influence region, for a parcel with angle $d\theta$, the number of association bonds is

$$dN_b=\frac{1}{2}[(r+vdt)^2-r^2]d\theta P_{\mathrm{on}}n_r. \tag{10}$$

Because the ligand density is about two times higher than that of the receptor, receptors in the influence region are expected to be fully saturated [10], and this estimation is confirmed in our numerical studies through counting the number of active bonds (cf. Appendix A). The biological bond, in general, assumes an arbitrary angle with the substrate. For example, the closed bonds should demonstrate stochastic directions. However, this cannot apply to the bonds in the influence region. The angle of a bond will be around $\pi/2$ in the influence region at the leading edge. Because, for a specific ligand on the NP, the newly created bond forms in the vertical direction with high probability as the distance is minimum under this

circumstance, leading to a lower energy state of the LRB. Similarly, in the limited influence region at the trailing edge, the bonds will be stretched compared to their last state. And those bonds with angles larger or smaller than $\pi/2$ for specific ligands suffer a high probability to break up before stretching. Hence, the bonds in the influence regions are assumed to be in vertical direction (shear direction). To further validate this scenario, the resultant bond force in the simulation is calculated. It reveals that the bond force in the flow direction is nearly zero, though there is a small increase for the cases with a large moving velocity of NP (cf. Appendix A). Therefore, we only consider the bond force in the shear direction and it can be expressed as $F^b = k_s(x - \delta_{\text{eq}})$. The arm of the bond force is $L = r\sin\theta$, then we have the torque on NP exerted by the association bonds $dM_{\text{on}} = \int_0^{\pi} dN_b L F^b$. Ignoring the second order $(dt)^2$, we have association torque

$$M_{\text{on}} = \int_0^{t_s} 2r^2 v P_{\text{on}} n_r k_s (x - \delta_{\text{eq}}) dt. \tag{11}$$

Similarly, we can obtain the dissociation torque

$$M_{\text{off}} = \int_0^{t_s} 2r^2 v P_{\text{off}} n_r k_s (x - \delta_{\text{eq}}) dt, \tag{12}$$

but here $x = R(1 - \cos(\beta_0 - \beta^* + \frac{vdt}{R})) + \delta_{\text{eq}}$, where $\beta^* = \frac{vt_s}{R}$ corresponds to the angle of NP's rotation within time t_s. The integration time t_s should reflect the kinetics of interactions between ligands and receptors. Here, k^0_{on} and k^0_{off} characterize the LRB process. According to the experiment [41], the association rate k^0_{on} is typically few orders of magnitude larger than the dissociation rate k^0_{off}. The fast association process is difficult to capture, and is not of significant when considering flow with small shear rate. Therefore, k^0_{off} is adopted to quantify the LRB process, and the integration time t_s is chosen as $1/k^0_{\text{off}}$. Eventually, we obtain the torque due to LRB as

$$M_{\text{LR}} = M_{\text{off}} - M_{\text{on}}. \tag{13}$$

3. Numerical Formulation

In the numerical simulation, the Lattice Boltzmann method (LBM) is adopted to solve the fluid flow, which is an efficient and accurate method for fluid dynamics [42]. The linearized Boltzmann equation has the form of:

$$(\partial_t + e_{\text{i}\alpha}\partial_\alpha) f_i = -\frac{1}{\tau}(f_i - f_i^{eq}) + F_i, \tag{14}$$

where $f_i(\mathbf{x}, t)$ is the distribution function for fluid particles with velocity $\mathbf{e}_i$ at position $\mathbf{x}$ and time t, $f_i^{eq}(\mathbf{x}, t)$ is the equilibrium distribution function and τ is the non-dimensional relaxation time, F_i is an external forcing term. In this simulation scheme, D3Q19 model is

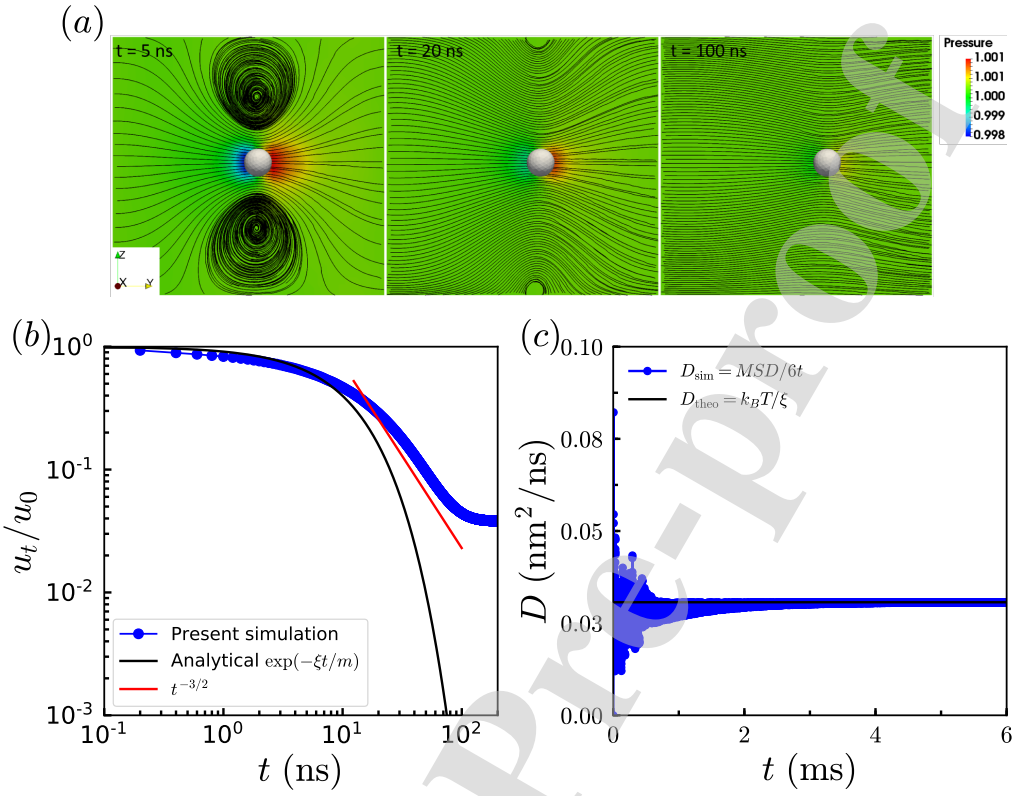

Figure 2: Validation for the motion of a nanoparticle (NP) in thermal-fluid environment. (a) Snapshots of streamlines around the NP, which freely translates in quiescent flow with initial velocity u_0. The contour presents the pressure of the flow field. (b) Relaxation of normalized NP velocity u_t/u_0. (c) Evolution of diffusion coefficient of NP immersed in the thermal fluid with temperature $T = 310$ K.

used [43]. The equilibrium distribution function $f_i^{eq}(\mathbf{x}, t)$ can be calculated as: $f_i^{eq}(\mathbf{x}, t) = \omega_i \rho \left[1 + \frac{\mathbf{e}_i \cdot \mathbf{u}}{c_s^2} + \frac{(\mathbf{e}_i \cdot \mathbf{u})^2}{2c_s^4} - \frac{(\mathbf{u})^2}{2c_s^2}\right]$, where the weighting coefficients $\omega_i = 1/3\ (i = 0), \omega_i = 1/18\ (i = 1-6), \omega_i = 1/36\ (i = 7-18)$. The term c_s represents the sound speed which equals $\Delta x/(\sqrt{3}\Delta t)$. The relaxation time is related to the kinematic viscosity in Navier-Stokes equation in the form of $\nu = (\tau - \frac{1}{2})c_s^2 \Delta t$. The external forcing term can be discretized as [44]: $F_i = (1 - \frac{1}{2\tau})\omega_i \left[\frac{\mathbf{e}_i - \mathbf{u}}{c_s^2} + \frac{(\mathbf{e}_i \cdot \mathbf{u})}{c_s^4}\mathbf{e}_i\right] \cdot \mathbf{F}$. Eq. (14) is solved by the integration algorithm proposed by [45]. Once the particle density distributions are known, the fluid density and momentum are calculated as

$$\rho = \sum_i f_i, \ \ \rho \mathbf{u} = \sum_i f_i \mathbf{e}_i + \frac{1}{2}\mathbf{F}\Delta t. \tag{15}$$

The NP is represented by a rigid spherical shell with surface uniformly discretized into

N nodes, e.g, $N = 726$ for $R = 40$ nm. To couple the NP with surrounding fluid flow, a dissipative force $\mathbf{F}_d = \xi(\mathbf{v} - \mathbf{u})$ is introduced and exerted on both fluid nodes and NP nodes. ξ is the damping coefficient. $\mathbf{v}$ is the velocity of the NP node, and $\mathbf{u}$ is the velocity of the fluid at the same location as the NP node. Because the fluid flow is described in Cartesian mesh and the fluid nodes are fixed, $\mathbf{u}$ should be interpolated by the surrounding fluid nodes. Based on the immersed boundary method [46], a smoothing kernel is adopted to interpolate the surrounding fluid nodes to the location of NP nodes.

$$\mathbf{u}(\mathbf{X}, t) = \int_{\Omega} \mathbf{u}(\mathbf{x}, t)\delta(\mathbf{x} - \mathbf{x}(\mathbf{X}, t))d\Omega, \tag{16}$$

where x and X denote fluid node and NP node, respectively. We use a 4 point approximation to the Dirac delta function, providing a support of 64 grid nodes

$$\delta(x) = \begin{cases} \frac{1}{8}(3 - 2|x| + \sqrt{1 + 4|x| - 4x^2}), & 0 \le |x| \le 1, \\ \frac{1}{8}(5 - 2|x| + \sqrt{-7 + 12|x| - 4x^2}), & 1 \le |x| \le 2, \\ 0, & 2 \le |x|. \end{cases} \tag{17}$$

The dissipative force $\mathbf{F}_d$ is directly applied to the NP nodes, and the motion of NP is driven by the resultant force and torque. In addition, to reflect the existence of a NP in the fluid flow, $\mathbf{F}_d$ is also spread into the surrounding fluid nodes. And the same smoothing kernel as the interpolation of velocity should be used. Although this numerical scheme about the particle-fluid coupling has been validated in [43] and our previous works [47, 48, 20], we further validate it using the case of translation of a single NP in quiescent fluid. The NP is placed in the center of a cubic domain of side length $24R$ with initial velocity u_0. As shown in Fig. 2(a), at time $t = 5$ ns, a starting recirculation flow structure is observed, which is also reported in [49]. It demonstrates the strong momentum transfer between the flow and NP. At $t = 20$ ns, the momentum transfer becomes weak, and the radius of curvature of streamlines becomes larger. Eventually, at time $t = 100$ ns, the streamlines become parallel to each other, and there is no momentum transfer between the NP and surrounding fluid flow. We plot the evolution of NP's velocity in Fig. 2(b). It indicates that, for a short time $t < 40$, the velocity of NP presents analytical exponential decay $\exp(\frac{\xi t}{m})$, where m is the mass of NP. In the long time regime, we also find the power decay $t^{-3/2}$, which was pointed out in [49]. This long-time tail decay behavior is due to the hydrodynamic interaction between the NP and flow field. These good agreements demonstrate the accuracy of the hydrodynamic coupling between NP and fluid field. More details about our numerical scheme and implementation can be found in [48].

The thermal fluctuation of the system is accounted for by introducing Gaussian white noise [50]. The fluctuation stress tensor $s_{\alpha\beta}$ satisfies a fluctuation dissipation relation with the form

$$\langle s_{\alpha\beta}(\mathbf{r}, t)s_{\gamma\nu}(\mathbf{r}', t')\rangle = 2\eta k_B T(\delta_{\alpha\gamma}\delta_{\beta\nu} + \delta_{\alpha\nu}\delta_{\beta\gamma})\delta(\mathbf{r}\text{-}\mathbf{r}')\delta(t - t'), \tag{18}$$

where $\mathbf{r}$ is the position of the fluid node and δ_{ij} is the Kroneckers symbol. With the same setup of the movement of NP in quiescent fluid, we apply thermal perturbation with temperature

$T = 310\ K$ instead of initial velocity u_0. With the thermal effect, the NP will make stochastic motion, and we calculate the time-averaged mean squared displacement (MSD) with the definition $MSD = \langle(\mathbf{r}_i - \mathbf{r}_0)^2\rangle$. $\langle\ \cdot\ \rangle$ represents the ensemble average of experiments for a single particle in the fluid flow. For a self-diffused Brownian particle in quiescent fluid, the diffusion coefficient D_{theo} is predicted by the theoretical analysis in [51] that $D_{\text{theo}} = k_B T/\xi$. We also calculate the diffusion coefficient D_{sim} in the simulation with $D_{\text{sim}} = MSD/6t$, and the evolution of D_{sim} is presented together with D_{theo} in the Fig. 2(c). It is found that, after a short transition, D_{sim} converges to the theoretical prediction D_{theo}. This confirms that the thermal perturbation added into the fluid model is accurate to capture the Brownian motion of the NP. Other validations for the thermal fluctuation are referred to [43].

For the LRB process, each node distributed on the NP surface denotes a ligand. And the receptors are illustrated by the nodes distributed with a square pattern on the substrate. The biological bonds formed between ligands and receptors are controlled by the stochastic model (Eq. (9)). The specific validations of this model have detailed in the work of [47].

4. Results and Discussion

4.1. Motion of the NP on the substrate

According to Eq. (7), the motion of NP is governed by the balance between LRB torque and hydrodynamic torque. To quantify the torques with relation to NP's velocity v, we first integrate the expression of M_{on} and M_{off} from analytical equations Eq. (11) and Eq. (12), respectively. Fig. 3(a) shows the results of a typical case of $R = 80$ nm, $E_r = -45\ k_{\text{B}}T$ and other parameters given in Table 1. It is found that the association torque M_{on} demonstrates three stages with the increment of moving velocity v: i) extremely small when $v < 0.01$ nm/ns; ii) continuous increase in the regime 0.01 nm/ns $< v < 0.035$ nm/ns; and iii) approximately constant when $v > 0.035$ nm/ns. In the stage of extremely small, because v is very small, the influence region is narrow and the newly formed bonds are limited. Furthermore, part of the formed bonds will quickly become closed bonds due to the very large association rate k_{on}^0. Hence, the association torque M_{on} exerted on the NP is extremely small. With the increment of v and enlargement of influence region in the stage of continuous increase, more and more active bonds form in the leading edge, which makes the association torque M_{on} become significant and continuously increase. However, a further increase of v will lead to the saturation of newly formed bonds, resulting in the plateau of M_{on} (stage of approximately constant).

By contrast, only two stages are found for the dissociation torque M_{off}. The first stage is characterized by the dramatic increase of M_{off} with the increment of v ($v < 0.016$ nm/ns). And the second stage for M_{off} keeps almost constant and is unrelated to NP's velocity v, similar to the last stage of association torque M_{on}. In the first stage, the increase of moving velocity v, on the one hand, enlarges the influence region and thus more closed bonds are stretched, on the other hand, makes a single closed bond more stretched. These two factors

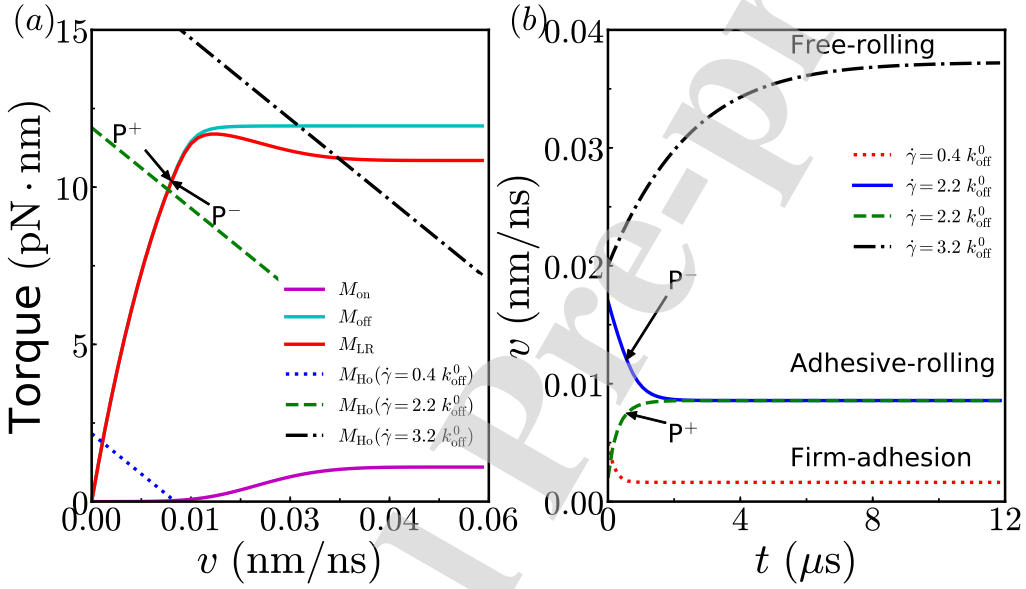

Figure 3: (a) Torques of association ($M_{\rm on}$), dissociation ($M_{\rm off}$), total ligand-receptor binding ($M_{\rm LR}$), and hydrodynamics ($M_{\rm Ho}$) with shear rates $\dot{\gamma} = 0.4, 2.2$ and $3.2\ k^0_{\rm off}$. P^+ and P^- represent that the initial velocity is smaller and larger than the steady velocity, respectively. (b) Velocity evolution of three types of motion for a spherical NP: Firm-adhesion ($\dot{\gamma} = 0.4\ k^0_{\rm off}$); Adhesive-rolling in P^+ and P^-($\dot{\gamma} = 2.2\ k^0_{\rm off}$); and free-rolling ($\dot{\gamma} = 3.2\ k^0_{\rm off}$).

result in the dramatic increase of M_{off}. Besides, a further increase of v makes the stretched bonds saturated and leads to saturation of M_{off}.

In order to compare the LRB torque M_{LR} and hydrodynamic torque $M_{\text{Ho}} = F_h R + M_h$, the M_{LR} is first obtained by Eq. (13) and presented in Fig. 3(a). M_{LR} is found to have three stages: i) dramatic increase; ii) small decrease; and iii) approximately constant with the increase of v. Among them, the stage of dramatic increase is dominated by the dissociation torque M_{off} and the stage of small decrease is attributed to the increase of association torque M_{on}.

Furthermore, the hydrodynamic torque M_{Ho} for cases with the same sized NP, but different flow strengths (shear rate $\dot{\gamma}$) are demonstrated in the same figure of M_{LR} (cf. Fig. 3(a)). Here, the shear rate $\dot{\gamma}$ is normalized by k_{off}^0 that characterizes the time scale of LRB process. According to Eq. (8), M_{Ho} monotonically decreases with the increase of v as shown in Fig. 3(a), and this makes the M_{LR} and M_{Ho} curves intersect at a specific point. The intersection means the balance of torques exerted on the NP and represents the steady state. Also, to investigate how the moving velocity evolves, we recall the time-dependent governing equation Eq. (6) and numerically integrate it. The evolution of moving velocity v is shown in Fig. 3(b) for corresponding cases. From Fig. 3(a), we find that when the flow is weak ($\dot{\gamma} = 0.4\ k_{\text{off}}^0$), the moving velocity v of NP is extremely low, and this steady state is called firm-adhesion (FA), in which the NP can hardly roll on the substrate. Under this circumstance, an initially high velocity of NP will continuously decrease and finally, it reaches the static state (FA, see Fig. 3(b)). When the shear rate increases to moderate ($\dot{\gamma} = 2.2\ k_{\text{off}}^0$), the flow strength is comparable with the strength of LRB, and the movement of NP becomes significant. The NP can always reach a steady rolling state, which is irrelevant to the initial velocity (high (P^-) or low (P^+), cf. Fig. 3(b)). We name this type of motion as adhesive-rolling (AR). With the further increase of flow strength, the intersection enters the regime where the M_{LR} is approximately constant and becomes irrelevant to the moving velocity v. Therefore, stronger flow ($\dot{\gamma} = 3.2\ k_{\text{off}}^0$) will lead to the hydrodynamics-dominated regime where the NP motion is determined by M_{Ho}. In this regime, even though the initial velocity is small, the strong flow will drive the NP to move and accelerate until the NP reaches a steady state (Fig. 3(b)). This freely moving motion is named free-rolling (FR).

4.2. $v - \dot{\gamma}$ curve: transitions of FA-to-AR and AR-to-FR

To further understand the relation between flow strength $\dot{\gamma}$ and moving velocity v of NP, we rewrite the governing equation Eq. (7) to isolate the LRB and hydrodynamics effects, and obtain the $\dot{\gamma} - v$ relation:

$$\dot{\gamma} = \frac{M_{\text{LR}}(v)}{\pi\eta a_1 R^2 (R + \delta_{\text{eq}})} + \frac{a_2}{a_1 (R + \delta_{\text{eq}})} v, \tag{19}$$

where $a_1 = 6F_s^* + 8T_s^*$ and $a_2 = 6F_t^* + 8T_r^*$. In Eq. (19), we define $\dot{\gamma} = \dot{\gamma}_l + \dot{\gamma}_h$, where $\dot{\gamma}_l = \frac{M_{\text{LR}}(v)}{\pi\eta a_1 R^2 (R+\delta_{\text{eq}})}$ and $\dot{\gamma}_h = \frac{a_2}{a_1 (R+\delta_{\text{eq}})} v$ characterize the LRB and hydrodynamics effects, respectively.

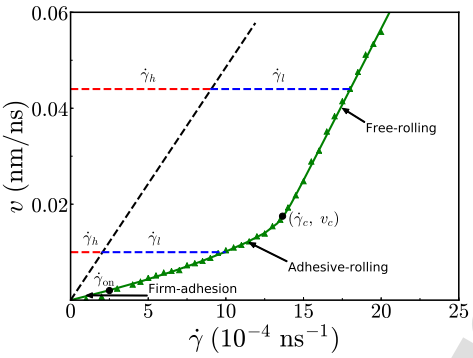

Figure 4: $v - \dot{\gamma}$ curve. Symbols represent the numerical simulation results. $\dot{\gamma}_{\rm on}$ shows the critical shear rate that NP starts to move on the substrate from static state. The critical point $(\dot{\gamma}_c, v_c)$ denotes the transition from AR to FR for the spherical NP. The black dashed line is the $v - \dot{\gamma}$ curve under the hydrodynamics without LRB.

We integrate the Eq. (19), and the analytical $v - \dot{\gamma}$ curve is presented in Fig. 4. To demonstrate $\dot{\gamma}_h$ and $\dot{\gamma}_l$, we also plot the $v - \dot{\gamma}$ curve for free-rolling of NP (black dashed line) under the circumstance that the NP is driven to freely move on the substrate only by shear flow. Then we can identify $\dot{\gamma}_h$ and $\dot{\gamma}_l$ as shown in Fig. 4. Furthermore, the simulation results (symbols) are presented in the same figure, which are in good agreement with theoretical predictions. The $v - \dot{\gamma}$ curve can be separated into three parts: i) v is very small; ii) v continuously increases; and iii) v dramatically increases with the increment of flow strength $\dot{\gamma}$. These three parts exactly correspond to the three types of motion: FA, AR, and FR respectively, which will be discussed below.

It should be noted that, in the FA regime, the simulation result demonstrates that the NP maintains its averaged static state under a low shear rate, which is slightly inconsistent with the theoretical analysis. This discrepancy is caused by the assumption that, in the theory, the NP is always expected to move on the substrate. However, the NP can start to move only when the flow strength exceeds a critical value ($\dot{\gamma} > \dot{\gamma}_{\rm on}$). It can be explained as follows. Without shear flow, the torques on the trailing and leading edges of NP are balanced in the static state. However, when the NP tends to move with the increment of the flow strength, the biological bonds on the trailing edge are strongly stretched while those on the leading edge are compressed, in comparison with their equilibrium state. The torque exerted on the NP induced by the biological bonds on the trailing edge is larger than that on the leading edge. This imbalance is named LRB barrier that hinders the start of the NP. Therefore, before NP can move, the LRB barrier should be overcome by the compensation from hydrodynamics through continuously increasing the flow strength, which is like mechanical static friction. Furthermore, we find that the critical shear rate $\dot{\gamma}_{\rm on}$ will decrease if the thermal fluctuation is considered in the simulation, which indicates the thermal fluctuation can lower the LRB barrier through introducing thermal torque (cf. Appendix B).

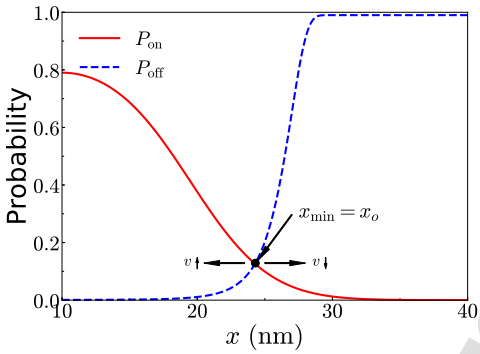

Figure 5: Illustration of the stochastic probability distribution against the bond length for ligand-receptor binding. P_{on} and P_{off} represent the association and dissociation probabilities, respectively. The intersection point between them denotes the position of x_{min} that is the minimum length of biological bond in the influence region.

In the second part of the $v - \dot{\gamma}$ curve (AR regime), the moving velocity v continuously increases with the increment of $\dot{\gamma}$. Comparing $\dot{\gamma}_h$ with $\dot{\gamma}_l$, we can see $\dot{\gamma}_l$ dramatically increases, while $\dot{\gamma}_h$ increases linearly, which subjects to free rolling motion. This means that the hydrodynamic torque increases to be comparable with the LRB torque. At this stage, only a small portion of the hydrodynamic torque is consumed to maintain the free-rolling-like motion, while the majority is used to balance the LRB torque.

However, the curve in the third part (FR regime) is found to be parallel to the free-rolling curve (black dashed line). In this part, the $\dot{\gamma}_l$ will be constant, which corresponds to the plateau stage of the LRB torque. On the contrary, the $\dot{\gamma}_h$ will continuously, though linearly, increase and exceed the $\dot{\gamma}_l$. Therefore, hydrodynamics will dominate the motion of free rolling.

In the transition from AR to FR, there should exist a critical velocity point ($\dot{\gamma}_c$, v_c). After this point, the moving of NP becomes irrelevant to LRB, which is due to the saturation of LRB torque and continuous increase of hydrodynamic torque with the increment of moving velocity shown in Fig. 3(a). Therefore, the critical velocity v_c corresponds to the maximum LRB torque. We have known that the dissociation torque M_{off} increases with the increment of v, and eventually reaches plateau regime. While association torque M_{on} slightly increases with the increment of v only after v reaches the relatively large value, and then also becomes approximately constant. Hence, the maximum of LRB torque occurs when M_{off} reaches maximum and M_{on} slightly increases. To determine this critical point, we consider the essential parts of association and dissociation probabilities P_{on} and P_{off}. Fig. 5 presents the probabilities that are dependent on the length of biological bond. We define x_o as the length of bond where $P_{on} = P_{off}$ and x_{min} that corresponds to β^* which points to the minimum length of biological bond in the influence region on trailing edge. At velocity $v = v_c$, we let $x_{min} = x_o$. When v increases, x_{min} will be smaller than x_o. Although P_{off} is

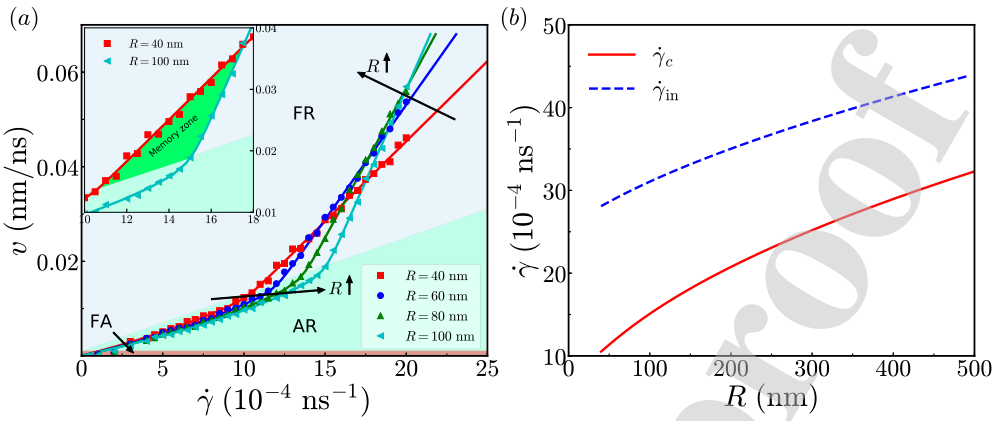

Figure 6: (a) $v - \dot{\gamma}$ curves for NPs with $R = 40, 60, 80$, and 100 nm, and simulation results are denoted by symbols. The $v - \dot{\gamma}$ plane are split into three parts: FA (red); AR (green); and FR (grey). The arrows guide the direction for the increase of NP size in AR and FR regions. The inserted figure represents the zoom-in of memory zone between NPs of $R = 40$ nm and $R = 100$ nm. (b) The shear rates for critical point $\dot{\gamma}_c$ and intersection point $\dot{\gamma}_{in}$ against the radius of NP.

lower, the influence region will enlarge a little and dissociation torque M_{off} will have a small increase. However, the association probability P_{on} has a substantial increase, which leads to the significance of association torque M_{on}. Therefore, LRB torque will decrease under this circumstance. When v decreases, x_{min} will be larger than x_o. Although P_{off} increases, the influence region will shrink and less closed bonds will be stretched, which results in the decrease of dissociation torque M_{off}. And the decrease of P_{on} makes the association torque M_{on} negligible. Hence, LRB torque will also decrease in this case. Combining the above two aspects, we can determine that the bond length at the intersection point between P_{on} and P_{off} should be the minimum length of biological bond (x_{min}) in the influence region, which corresponds to the maximum LRB torque. Furthermore, according to the relation between β^* and x_{min}, we can obtain the critical velocity

$$v_c(R) = \frac{R}{t_s}(\beta_0 - \arccos(1 - \frac{x_{min} - \delta_{eq}}{R})). \tag{20}$$

It is found that the critical velocity v_c is strongly dependent on the radius R of NP, which means different sized NPs have different critical velocity points for the transition from AR to FR. In the next section, we will further study the effect of NP size in both AR and FR regimes.

4.3. Size dependence: smaller moves faster

To quantify the motion of different sized NPs, we conduct three more cases with the radii $R = 40, 60$, and 100 nm. The corresponding $v - \dot{\gamma}$ curves are presented in Fig. 6(a).

Except for the FA regime, they have different performances in both AR and FR regimes. In the regime of AR, we find that the smaller NP moves faster than the larger ones under the same flow strength. This is counter-intuitive as Stokes' prediction says the larger particle will move faster than the smaller one in the same flow. However, the inclusion of LRB process breaks this prediction and predicts the opposite result in the AR regime. Furthermore, the critical points of the transition from AR to FR vary with the radius of NP, which has been confirmed by Eq. (20). The corresponding critical shear rates $\dot{\gamma}_{\mathrm{c}}$ are also calculated based on the expression of v_c (Eq. (20)). It is plotted against the radius of NP in Fig. 6(b). We find that the larger the NP is, the higher the critical shear rate will be, which indicates the stronger flow is needed to drive the larger NP to move with the same velocity as the smaller one.

The critical points for different sized NPs together consist of the critical $v - \dot{\gamma}$ curve. We put this curve in Fig. 6(a) and it illustrates the boundary between the AR and FR regimes. The $v - \dot{\gamma}$ plane is further split into two main regions: AR (green) and FR (grey) plus a narrow FA region (red).

In the FR region, the motion of NP is dominated by the hydrodynamics, which recalls the Stokes' prediction that larger NP moves faster than the smaller one. However, it is not true in the whole FR region. Since the critical point depends on the size of NP, larger NP has higher moving velocity when entering FR region compared to the smaller one. Therefore, at the initial stage of the FR region where different sized NPs enter FR regime, the smaller one can still move faster than the larger one. For example, we zoom into the initial stage of FR region for the cases $R = 40$ nm and $R = 100$ nm. It is clear that, for the same flow strength, the smaller NP ($R = 40$ nm) moves faster than the larger one ($R = 100$ nm). However, further increment of the flow strength will make the larger NP exceed the smaller one. Therefore, there is a closed region between the critical $v - \dot{\gamma}$ curve, the $v - \dot{\gamma}$ curve for $R = 40$ nm and the $v - \dot{\gamma}$ curve for $R = 100$ nm, as denoted in the inserted zoom-in figure. We name this region as memory zone where LRB torque still exists and contributes to the motion of NP, though it keeps constant. It is found that the larger size difference between NPs is, the larger the memory zone will be. It means that, compared to a specific small NP ($R = 40$ nm), if the size of the other NP is larger, higher hydrodynamic torque is required to compensate for the LRB torque and eliminate the memory.

However, the memory of LRB will become negligible when the hydrodynamic torque further increases and Stokes' predication is fully recovered. It is characterized by the intersection of two $v - \dot{\gamma}$ curves of different sized NPs. Assuming two NPs with radii R_1 and R_2, their shear rates can be expressed as

$$\dot{\gamma}_{\mathrm{R}_i} = \frac{A}{R_i} v + \dot{\gamma}_{\mathrm{c}}|_{v=v_{\mathrm{c}}(R_i)}, \ i = 1, 2, \tag{21}$$

where $A = a_2/a_1$. At the intersection point, $\dot{\gamma}_{\mathrm{R}_1} = \dot{\gamma}_{\mathrm{R}_2}$, then we have the velocity

$$v_{\mathrm{in}} = \frac{\dot{\gamma}_{\mathrm{c}}(R_2) - \dot{\gamma}_{\mathrm{c}}(R_1)}{A(\frac{1}{R_1} - \frac{1}{R_2})}. \tag{22}$$

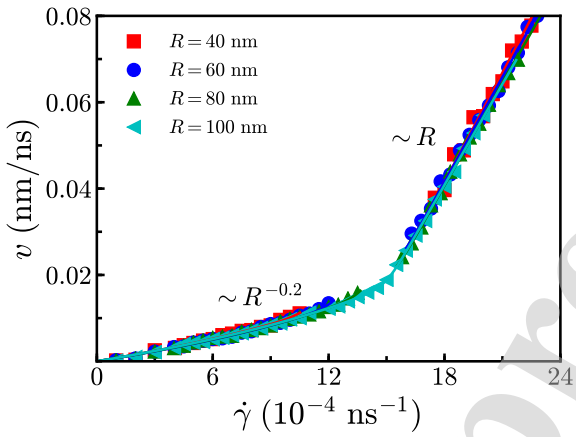

Figure 7: $v - \dot{\gamma}$ scaling with respect to radius R of NP. The scaling laws are $\sim R^{\alpha}$ and $\sim R$ in AR and FR regions, respectively.

Finally, we can have the $\dot{\gamma}_{\text{in}}$ based on the $v - \dot{\gamma}$ relation. Furthermore, we adopt the case of $R_2 = 500$ nm as a reference, and plot the $\dot{\gamma}_{\text{in}}$ against the radius of NP in Fig. 6(b). It is found that $\dot{\gamma}_{\text{in}}$ increases with the increment of NP radius, which illustrates that the smaller NP will be easier to exceed the referenced one ($R_2 = 500$ nm) in the FR regime.

4.4. Universal size scaling law

The NP size has demonstrated different influences in the AR and FR regions. Compared to the relation $v \propto \dot{\gamma} R$ in the FR region, the $v - \dot{\gamma}$ relation in the AR region remains to be further explored due to the complex expression of LRB torque with respect to v. In the $v - \dot{\gamma}$ plane, the $v - \dot{\gamma}$ curves of different sized NPs are scaled with respect to the reference ($R = 100$ nm). By fitting both theoretical and numerical results, we find that there exists a scaling factor $\alpha \approx -0.2 \pm 0.04$ that can make all $v - \dot{\gamma}$ curves approximately collapse into that of the referenced NP. Furthermore, to have a consistent view, the $v - \dot{\gamma}$ curves are also scaled in the FR region according to scaling $\sim R$. And we find all the $v - \dot{\gamma}$ curves will be parallel to each other. The vertical shift between the scaled curves is caused by the different critical points $(v_c, \dot{\gamma}_c)$ that depend on the radii of NPs. Nevertheless, they can collapse together through vertical shifting with the distances that are determined by the critical points. And the final results are presented in Fig. 7 with simulations results represented by symbols.

We have known that R scaling in the FR region stems from the hydrodynamics based on Stokes' prediction. To gain insights into R^{α} scaling in the AR region, we recall the expression of M_{LR}. It mainly consists of three parts that are relevant to the radius of NP: (i) area of influence region Σ; (ii) length of bond x; and (iii) association and dissociation probabilities P_{on} and P_{off}. Firstly, the area of influence region Σ scales to r^2, hence, we have $\Sigma \propto R^2$. Secondly, the length of bond $x \propto R$. According to Eq. (19), these two parts cancel R^3 and

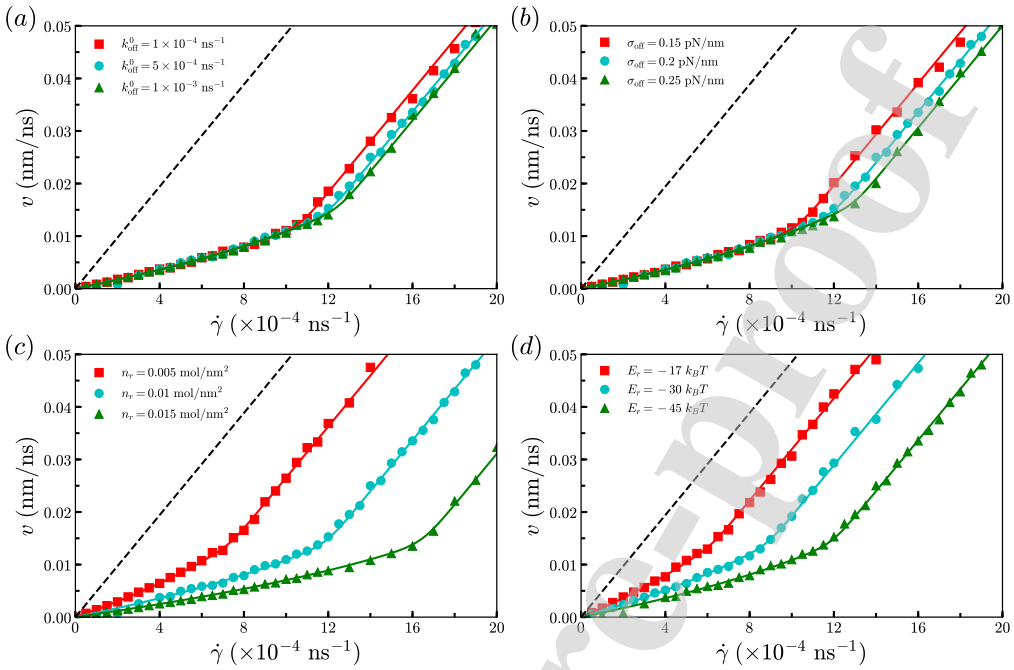

Figure 8: $v-\dot{\gamma}$ curves for NPs with different (a) dissociation rates $k^0_{\rm off}$ at equilibrium length, (b) effective off strengths $\sigma_{\rm off}$, (c) receptor densities n_r, and (d) rupture energies E_r of a single bond. Symbols in the figures represent the simulation results.

the scaling R^α should be mainly dependent on the last part – contributions of association and dissociation probabilities $P_{\rm on}$ and $P_{\rm off}$. In this work, the probabilities are established based on the energy of the bond $E_{\rm b}$, which is related to $(l-l_0)^2$. The dependence of R on the length of bond $l-l_0$ in these probabilities leads to the scaling factor α. Based on this analysis, the scaling can be also extended to the force-based adhesion model, in which the force is defined as $F^b = k_s(l-l_0)$. Although the scaling factor α is an approximation, it can still predict that smaller NP should move faster than the larger counterpart. This universal scaling law should direct all the stochastic model-based adhesive motion of NPs.

According to above discussions, the scaling law is determined to be relevant to the stochastic model of LRB. We further investigate the influence of important parameters in the probability model of LRB. Because the dissociation torque on the trailing edge dominates the LRB process, the dissociation rate $k^0_{\rm off}$ at the equilibrium length and effective off strength $\sigma_{\rm off}$ are systemically varied. The corresponding $v-\dot{\gamma}$ curves are presented in Fig. 8(a) and (b), respectively. In Fig. 8(a), it is found that $k^0_{\rm off}$ has negligible effect in the AR regime, while it affects the critical points of AR-to-FR transition. In Eq. (12), with the increase of dissociation rate $k^0_{\rm off}$, the dissociation probability $P_{\rm off}$ will increase. However, the integration time $t_s = 1/k_{\rm off}$ that characterizes the LRB timescale will decrease. Therefore, the increase of

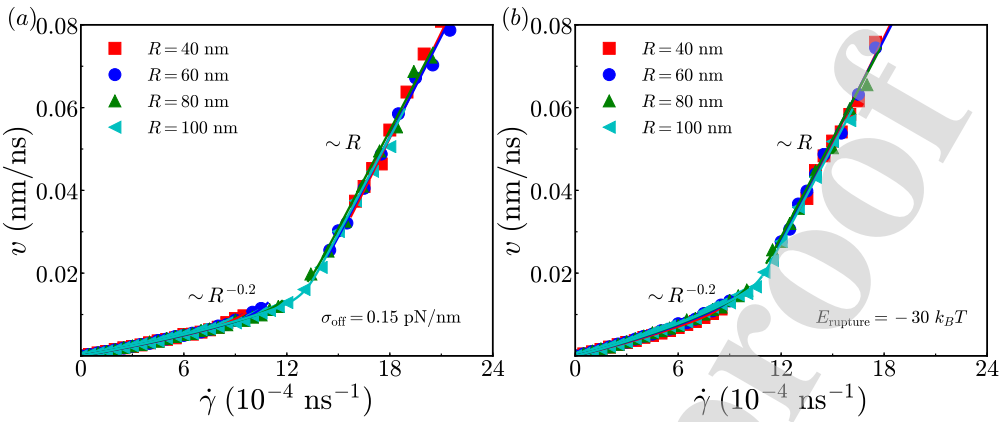

Figure 9: Influence of parameter selections on the $v-\dot{\gamma}$ scaling laws with respect to NP radius R: (a) effective off strength $\sigma_{\rm off}$ and (b) rupture energy E_r. Symbols in the figures represent the simulation results.

$k^0_{\rm off}$ cannot significantly affect dissociation torque. For the association torque on the leading edge, when NP's moving velocity is not large, the association probability $P_{\rm on}$ is small and the association torque can be negligible (cf. Fig. 3). Hence, when v is not large enough, $k^0_{\rm off}$ has negligible effect on the $v-\dot{\gamma}$ curve in the AR regime. However, when the moving velocity v increases to be close to the critical point, the association probability becomes significant. And the association torque decreases due to the decrease of the integration time t_s. Hence, the maximum LRB torque enhances with the increase of $k^0_{\rm off}$, which leads to the raise of the critical point. In Fig. 8(b), the effective off strength only affects the dissociation probability. When the moving velocity v is small, the term $\exp(\frac{\sigma_{\rm off}(l-l_0)^2}{2k_{\rm B}T})$ is small. The change of $\sigma_{\rm off}$ has negligible effect on $P_{\rm off}$ and thus has minimal effect on $v-\dot{\gamma}$ curve in the AR regime. However, when the moving velocity v is close to that at the critical point, the increase of $\sigma_{\rm off}$ will result in the significant increase of dissociation probability and the maximum LRB torque, which makes the right shift of the critical point as shown in the figure.

To further exclude the dependence of parameter selections, we study effects of receptor density n_r and rupture energy E_r as shown in Fig. 8(c) and (d), respectively. It is found that the receptor density n_r plays an important role in the AR region. For the same flow strength, the moving velocity v decreases with the increase of the receptor density. The increase of n_r leads to more bonds formed on the leading edge and more bonds are stretched on the trailing edge, which enlarges the LRB torque that inhibits the moving of NP on the substrate. Also, in Fig. 8(d), the rupture energy E_r denotes the strength of a single bond and higher rupture energy means stronger biological bond. The stronger bond will result in the larger LRB torque with the same number of bonds. Therefore, the moving velocity v of the NP will decrease with the increase of the rupture energy E_r for the same flow strength.

As $\sigma_{\rm off}$ and $k^0_{\rm off}$ have the same effects on the motion of NP in the AR region, we adopt $\sigma_{\rm off}$ to examine its dependence on the size scaling. Fig. 9(a) presents the size scaling result

for $\sigma_{\text{off}} = 0.15$ pN/nm. It is found that the scaling factor α also works well, which illustrates that the scaling law is irrelevant to the parameter selection of the probability model. Furthermore, we investigate the dependence of rupture energy E_r as a typical example of parameter selection in the model of torque M_{LR}. The scaling law is shown in Fig. 9(b) for $E_r = -30\ k_{\text{B}}T$. We find that the $v - \dot{\gamma}$ curves also collapse together with the factor α in the AR region. The examinations of parameter selections further confirm the universal size scaling law of NPs in the AR region as $v \propto \dot{\gamma} R^{\alpha}$ and $\alpha \sim -0.2 \pm 0.05$.

5. Conclusion

In the present work, both theoretical and numerical analyses are utilized to study the adhesive motion of a spherical NP on the substrate under LRB and shear flow. In the theoretical formulation, the motion of NP is governed by the interplay of hydrodynamics and LRB. The governing equation is subsequently derived through geometrical analysis and energy balance. It predicts three types of motion: FA, AR, and FR with the increase of flow strength. When the flow is weak (low $\dot{\gamma}$), the hydrodynamics is small compared to the LRB and the flow cannot drive the moving of NP. Moderate flow strength will make the hydrodynamics comparable with the LRB, which results in adhesive-rolling of NP. The FR regime is characterized by the strong flow strength that dominates the motion of NP. In this regime, the NP can freely move, which is like the motion of NP only under simple shear flow.

Between these three types of motion, two transitions are identified. The first transition is FA-to-AR. The reason why weak flow cannot drive the NP to move is the existence of LRB barrier. Only when the hydrodynamics overcomes the LRB barrier, the NP can start to move. The second transition is AR-to-FR. Due to the saturation of LRB torque, a continuous increase of flow strength will make hydrodynamics overwhelm the LRB, triggering the transition from AR to FR.

The motion of NP is also found to be strongly dependent on its radius. In particular, in the AR regime, the smaller NPs move faster than their larger counterparts. This conflicts with the Stokes' prediction that larger NP will move faster than the smaller one in the same shear flow. Furthermore, this contradiction is found to extend to the initial stage of the FR regime. Since the critical point that characterizes the transition of AR-to-FR depends on the size of NP, different sized NPs have different critical velocities. Therefore, there exists LRB memory zone between two different sized NPs. Stronger flow strength is required to eliminate the LRB memory for larger NP to pursue and exceed the smaller one. Finally, the Stokes' prediction can be fully recovered in the FR regime.

Besides, the size scaling law is found in the AR regime. Compared to the classical size scaling of $\sim R$ in the FR regime, an approximate scaling of $\sim R^{\alpha}$ is proposed and the scaling factor $\alpha \sim -0.2 \pm 0.05$ is quantified through fitting both theoretical and numerical results. By analyzing the expression of LRB torque, the size scaling is found to be relevant to the energy-based stochastic model. Furthermore, the size scaling is demonstrated to be universal regardless of the selection of parameters either in the LRB process or the shear flow.

According to the motion type of the NP under different shear rates, for a specific sized NP, such as SARS-COV-2 virus [2], the signal intensity can be enhanced through control of the shear rate to make more virus adhere or slowly moving within the observation window, instead of utilizing external stimulus like laser to amplify the signal. A corresponding design of LFD will help improve the reliability and quantification in the rapid antigen diagnostic tests. Furthermore, The size-dependent rolling behavior may open a broad application of LFD to detect various viruses with different sizes.

Acknowledgments

This work was mainly supported by the National Science Foundation (OAC-1755779). The authors acknowledge the Texas Advanced Computing Center (TACC) at The University of Texas at Austin for providing HPC resources (Frontera project and the National Science Foundation award 1818253) that have contributed to the research results reported within this paper. This work was partially supported by a fellowship grant (to H.Y. and Z.S.) from GEs Industrial Solutions Business Unit under a GE-UConn partnership agreement. The views and conclusions contained in this document are those of the authors and should not be interpreted as necessarily representing the official policies, either expressed or implied, of Industrial Solutions or UConn. This research benefited in part from the computational resources and staff contributions provided by the Booth Engineering Center for Advanced Technology (BECAT) at the University of Connecticut.

Declaration of Interests

The authors declare that they have no known competing financial interests or personal relationships that could have appeared to influence the work reported in this paper.

Appendix A. Validation of theoretical assumptions

In the setup of parameters related to the LRB process, the density of receptors on the substrate is two times lower than that of ligands on the NP surface. Therefore, we assume receptors on the substrate are saturated, which means that, inside the region on the substrate where receptors can interact with ligands, all the receptors will form bonds with corresponding ligands. Through projection of NP on the substrate, we can calculate the projection area A_0, hence, the number of active biological bonds should be $N_{\text{active}} = n_r A_0$ in the steady adhesive rolling state according to the theoretical assumption. To confirm this aspect, in the numerical simulations, we count the number of active biological bonds when the NP reaches steady state, and collect the results for different sized NPs, which is shown in Fig. A.10(a). From the comparison, the numerical results are consistent with the theoretical predictions, which confirms our theoretical assumption on saturation of receptors in the steady state regime.

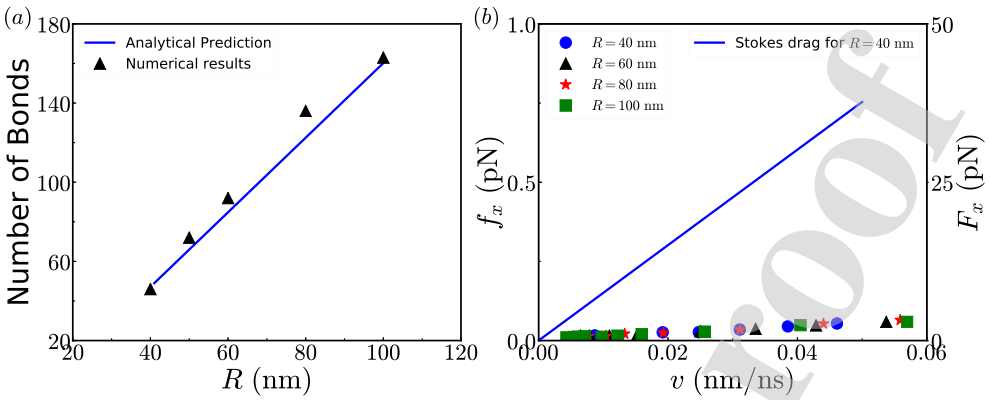

Figure A.10: (a) Comparison of theoretical predictions and numerical results of averaged number of active bonds for different sized NPs with radius R. (b) Resultant bond force f_x in the flow direction for different sized NPs under the steady motion with moving velocity v. The blue line denotes the Stokes drag force F_x of NP moving with velocity v.

The formation of biological bond between ligand and receptor is a stochastic process, therefore, the direction of the bond should be, in principle, assumed arbitrary. However, this has limited application to the bonds in influence region. The angles of these bonds should be around $\pi/2$ in the influence region on the leading edge, because those with other angles will break up due to larger length than the critical length d_{on}. This is also true for the bonds in the influence region on the trailing edge. To validate this aspect, in the simulation, we calculate the resultant bond force and show the force in the flow direction f_x in the Fig. A.10(b). It is found that, for different sized NPs, the force f_x is nearly zero, despite of the limited force for NPs moving with large velocity. For comparison, we also plot the Stokes' drag F_x of the NP with size $R = 40$ nm moving in the flow. It is obvious that the bond force that the NP experiences in the flow direction is negligible compared to the Stokes' drag. Therefore, it validates the assumption that the ligand-receptor bonds in the influence region is nearly vertical.

Appendix B.

In the simulation, we find that when the shear rate is lower than a critical value $\dot{\gamma}^*_{\text{on}}$, the NP demonstrates averaged static state as shown in Fig. B.11. This is not predicted in the theoretical analysis due to the assumption that NP is moving with velocity v. When $\dot{\gamma} > \dot{\gamma}^*_{\text{on}}$, the numerical results are consistent with the theoretical predictions. Furthermore, we consider the thermal fluctuation of the fluid. It is found that only when the moving velocity of NP is small, the thermal fluctuation has a significant effect on the motion of NP. This is because the Péclet number is small for low shear rate (slow moving particle). In addition, we find the critical shear rate $\dot{\gamma}_{\text{on}}$ is smaller than that without thermal fluctuation ($\dot{\gamma}_{\text{on}} < \dot{\gamma}^*_{\text{on}}$). It

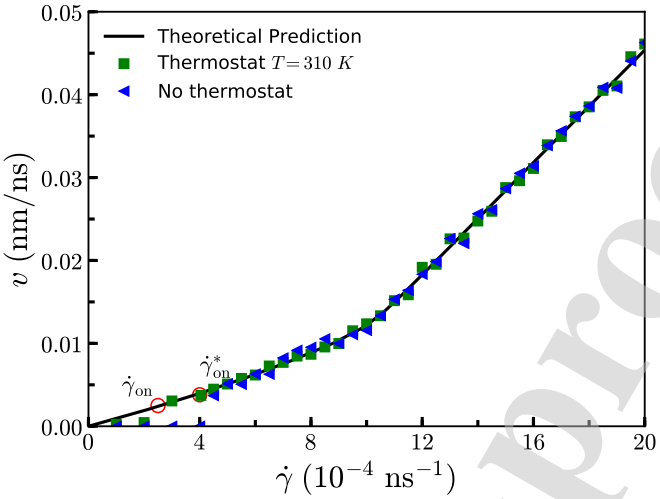

Figure B.11: Thermal fluctuation effect on the $v - \dot{\gamma}$ curve.

means the NP is easier to move under thermal fluctuation, which presents that the thermal fluctuation can help NP overcome the LRB barrier. With the increase of shear rate, the hydrodynamics is much stronger than thermal fluctuation. The thermal fluctuation effect cannot contribute to the regular motion of NP. Therefore, there is no significant difference between those with and without consideration of thermal fluctuation after NP starts to move.

References

[1] P. Zhou, X.-L. Yang, X.-G. Wang, B. Hu, L. Zhang, W. Zhang, H.-R. Si, Y. Zhu, B. Li, C.-L. Huang, et al., A pneumonia outbreak associated with a new coronavirus of probable bat origin, Nature 579 (7798) (2020) 270–273.

[2] A. N. Baker, S.-J. Richards, C. S. Guy, T. R. Congdon, M. Hasan, A. J. Zwetsloot, A. Gallo, J. R. Lewandowski, P. J. Stansfeld, A. Straube, et al., The sars-cov-2 spike protein binds sialic acids and enables rapid detection in a lateral flow point of care diagnostic device, ACS Cent. Sci. (2020) 591–605.

[3] C. C. Ginocchio, A. J. McAdam, Current best practices for respiratory virus testing, J. Clin. Microbiol. 49 (2011) 44–48.

[4] B. Pinsky, R. Hayden, Cost-effective respiratory virus testing, J. Clin. Microbiol. 57 (9) (2019) e00373–19.

[5] M. Soler, M. C. Estevez, M. Cardenosa-Rubio, A. Astua, L. M. Lechuga, How nanophotonic label-free biosensors can contribute to rapid and massive diagnostics of respiratory virus infections: Covid-19 case, ACS Sens. 5 (9) (2020) 2663–2678.

[6] H. Ye, Y. Liu, L. Zhan, Y. Liu, Z. Qin, Signal amplification and quantification on lateral flow assays by laser excitation of plasmonic nanomaterials, Theranostics 10 (10) (2020) 4359.

[7] L. J. Carter, L. V. Garner, J. W. Smoot, Y. Li, Q. Zhou, C. J. Saveson, J. M. Sasso, A. C. Gregg, D. J. Soares, T. R. Beskid, et al., Assay techniques and test development for covid-19 diagnosis, ACS Cent. Sci. 6 (2020) 591–605.

[8] K. Basile, J. Kok, D. E. Dwyer, Point-of-care diagnostics for respiratory viral infections, Expert Rev. Mol. Diagn. 18 (1) (2018) 75–83.

[9] J. B. Haun, D. A. Hammer, Quantifying nanoparticle adhesion mediated by specific molecular interactions, Langmuir 24 (16) (2008) 8821–8832.

[10] P. Decuzzi, M. Ferrari, The adhesive strength of non-spherical particles mediated by specific interactions, Biomaterials 27 (30) (2006) 5307–5314.

[11] P. Decuzzi, M. Ferrari, The role of specific and non-specific interactions in receptor-mediated endocytosis of nanoparticles, Biomaterials 28 (18) (2007) 2915–2922.

[12] S. Shah, Y. Liu, W. Hu, J. Gao, Modeling particle shape-dependent dynamics in nanomedicine, J. Nanosci. Nanotechnol. 11 (2) (2011) 919–928.

[13] J. Tan, A. Thomas, Y. Liu, Influence of red blood cells on nanoparticle targeted delivery in microcirculation, Soft Matter 8 (6) (2012) 1934–1946.

[14] Y. Li, W. Stroberg, T.-R. Lee, H. S. Kim, H. Man, D. Ho, P. Decuzzi, W. K. Liu, Multiscale modeling and uncertainty quantification in nanoparticle-mediated drug/gene delivery, Comput. Mech. 53 (3) (2014) 511–537.

[15] K. Vahidkhah, P. Bagchi, Microparticle shape effects on margination, near-wall dynamics and adhesion in a three-dimensional simulation of red blood cell suspension, Soft Matter 11 (11) (2015) 2097–2109.

[16] Z. Liu, J. R. Clausen, R. R. Rao, C. K. Aidun, Nanoparticle diffusion in sheared cellular blood flow, J. Fluid Mech. 871 (2019) 636–667.

[17] H. Vitoshkin, H.-Y. Yu, D. M. Eckmann, P. S. Ayyaswamy, R. Radhakrishnan, Nanoparticle stochastic motion in the inertial regime and hydrodynamic interactions close to a cylindrical wall, Phys. Rev. Fluids 1 (5) (2016) 054104.

[18] N. Ramakrishnan, Y. Wang, D. M. Eckmann, P. S. Ayyaswamy, R. Radhakrishnan, Motion of a nano-spheroid in a cylindrical vessel flow: Brownian and hydrodynamic interactions, J. Fluid Mech. 821 (2017) 117–152.

[19] A. Mozaffari, N. Sharifi-Mood, J. Koplik, C. Maldarelli, Self-propelled colloidal particle near a planar wall: A brownian dynamics study, Phys. Rev. Fluids 3 (1) (2018) 014104.

[20] H. Ye, Z. Shen, Y. Li, Interplay of deformability and adhesion on localization of elastic micro-particles in blood flow, J. Fluid Mech. 861 (2019) 55–87.

[21] H. Ye, Z. Shen, Y. Li, Shape-dependent transport of microparticles in blood flow: From margination to adhesion, J. Eng. Mech. 145 (4) (2019) 04019021.

[22] C. E. Chan, D. J. Odde, Traction dynamics of filopodia on compliant substrates, Science 322 (5908) (2008) 1687–1691.

[23] C.-M. Lo, H.-B. Wang, M. Dembo, Y.-l. Wang, Cell movement is guided by the rigidity of the substrate, Biophys. J. 79 (1) (2000) 144–152.

[24] A. J. Engler, S. Sen, H. L. Sweeney, D. E. Discher, Matrix elasticity directs stem cell lineage specification, Cell 126 (4) (2006) 677–689.

[25] E. Kolaczkowska, P. Kubes, Neutrophil recruitment and function in health and inflammation, Nat. Rev. Immunol. 13 (3) (2013) 159–175.

[26] K.-C. Chang, D. F. Tees, D. A. Hammer, The state diagram for cell adhesion under flow: leukocyte rolling and firm adhesion, Proc. Natl. Acad. Sci. U.S.A 97 (21) (2000) 11262–11267.

[27] R. Alon, S. Chen, K. D. Puri, E. B. Finger, T. A. Springer, The kinetics of l-selectin tethers and the mechanics of selectin-mediated rolling, J. Cell Biol. 138 (5) (1997) 1169–1180.

[28] A. Efremov, J. Cao, Bistability of cell adhesion in shear flow, Biophys. J. 101 (5) (2011) 1032–1040.

[29] X. Xu, A. K. Efremov, A. Li, L. Lai, M. Dao, C. T. Lim, J. Cao, Probing the cytoadherence of malaria infected red blood cells under flow, PLoS One 8 (5).

[30] L. Li, H. Tang, J. Wang, J. Lin, H. Yao, Rolling adhesion of cell in shear flow: a theoretical model, J. Mech. Phys. Solids 119 (2018) 369–381.

[31] A. Goldman, R. Cox, H. Brenner, Slow viscous motion of a sphere parallel to a plane wall—ii couette flow, Chem. Eng. Sci. 22 (4) (1967) 653–660.

[32] L. Landau, E. Lifshitz, Course of theoretical physics. vol. 6: Fluid mechanics, London, 1959.

[33] D. A. Hammer, S. M. Apte, Simulation of cell rolling and adhesion on surfaces in shear flow: general results and analysis of selectin-mediated neutrophil adhesion, Biophys. J. 63 (1) (1992) 35–57.

[34] G. I. Bell, Models for the specific adhesion of cells to cells, Science 200 (4342) (1978) 618–627.

[35] J. Qian, J. Wang, H. Gao, Lifetime and strength of adhesive molecular bond clusters between elastic media, Langmuir 24 (4) (2008) 1262–1270.

[36] D. A. Fedosov, B. Caswell, G. E. Karniadakis, Wall shear stress-based model for adhesive dynamics of red blood cells in malaria, Biophys. J. 100 (9) (2011) 2084–2093.

[37] D. Fedosov, B. Caswell, S. Suresh, G. Karniadakis, Quantifying the biophysical characteristics of plasmodium-falciparum-parasitized red blood cells in microcirculation, Proc. Natl. Acad. Sci. U.S.A 108 (1) (2011) 35–39.

[38] G. S. Longo, D. H. Thompson, I. Szleifer, Ligand- receptor interactions between surfaces: the role of binary polymer spacers, Langmuir 24 (18) (2008) 10324–10333.

[39] D. A. Fedosov, Multiscale modeling of blood flow and soft matter, Citeseer, 2010.

[40] M. Dembo, D. Torney, K. Saxman, D. Hammer, The reaction-limited kinetics of membrane-to-surface adhesion and detachment, Proc. R. Soc. Lond. B 234 (1274) (1988) 55–83.

[41] J. Hu, R. Lipowsky, T. R. Weikl, Binding constants of membrane-anchored receptors and ligands depend strongly on the nanoscale roughness of membranes, Proc. Natl. Acad. Sci. U.S.A (2013) 201305766.

[42] S. Chen, G. D. Doolen, Lattice boltzmann method for fluid flows, Annu. Rev. Fluid Mech. 30 (1) (1998) 329–364.

[43] F. Mackay, S. T. Ollila, C. Denniston, Hydrodynamic forces implemented into lammps through a lattice-boltzmann fluid, Comput. Phys. Commun. 184 (8) (2013) 2021–2031.

[44] Z. Guo, C. Zheng, B. Shi, Discrete lattice effects on the forcing term in the lattice boltzmann method, Phys. Rev. E 65 (4) (2002) 046308.

[45] S. T. Ollila, C. Denniston, M. Karttunen, T. Ala-Nissila, Fluctuating lattice-boltzmann model for complex fluids, J. Chem. Phys. 134 (6) (2011) 064902.

[46] C. S. Peskin, The immersed boundary method, Acta Numer. 11 (2002) 479–517.

[47] H. Ye, Z. Shen, Y. Li, Cell stiffness governs its adhesion dynamics on substrate under shear flow, IEEE Trans. Nanotechnol. 17 (3) (2018) 407–411.

[48] H. Ye, Z. Shen, Y. Li, Computational modeling of magnetic particle margination within blood flow through lammps, Comput. Mech. 62 (3) (2018) 457–476.

[49] B. Alder, T. Wainwright, Decay of the velocity autocorrelation function, Phys. Rev. A 1 (1) (1970) 18.

[50] A. M. Kopacz, N. A. Patankar, W. K. Liu, The immersed molecular finite element method, Comput. Methods Appl. Mech. Eng. 233 (2012) 28–39.

[51] A. Einstein, On the movement of small particles suspended in stationary liquids required by the molecularkinetic theory of heat, Ann D Phys 17 (1905) 1.

Declaration of Competing Interest

The authors declare that they have no known competing financial interests or personal relationships that could have appeared to influence the work reported in this paper.